JGR Solid Earth

RESEARCH ARTICLE
10.1029/2022JB025169

Experimental Constraints on the Fate of Subducted Sedimentary Nitrogen in the Reduced Mantle

Shengxuan Huang[1], Xiang Wu[2], Stella Chariton[3], Vitali B. Prakapenka[3], Lin Liang[1], Dongzhou Zhang[3,4], Yan Yang[5], Bin Chen[4], and Shan Qin[1]

[1]Key Laboratory of Orogenic Belts and Crustal Evolution, MOE, Peking University and School of Earth and Space Sciences, Peking University, Beijing, China, [2]State Key Laboratory of Geological Processes and Mineral Resources, China University of Geosciences, Wuhan, China, [3]Center for Advanced Radiation Sources, University of Chicago, Chicago, IL, USA, [4]Hawai'i Institute of Geophysics and Planetology, University of Hawai'i at Mānoa, Honolulu, HI, USA, [5]School of Earth Sciences, Zhejiang University, Hangzhou, China

Key Points:

- Subducted N-bearing silicates and fluids react with Fe or FeS to form different products at high *P-T* conditions
- Stability of Fe-LEs to 35 GPa and 1600 K is Fe-O > Fe-N > Fe-S > Fe-C, explaining the distribution of nitrides in diamonds
- The recycling efficiency of subducted sedimentary N is strongly related to the availability of the metallic Fe of the reduced mantle

Supporting Information:

Supporting Information may be found in the online version of this article.

Correspondence to:

X. Wu and S. Qin,
wuxiang@cug.edu.cn;
sqin@pku.edu.cn

Citation:

Huang, S., Wu, X., Chariton, S., Prakapenka, V. B., Liang, L., Zhang, D., et al. (2022). Experimental constraints on the fate of subducted sedimentary nitrogen in the reduced mantle. *Journal of Geophysical Research: Solid Earth*, *127*, e2022JB025169. https://doi.org/10.1029/2022JB025169

Received 12 JUL 2022
Accepted 11 NOV 2022

Author Contributions:

Conceptualization: Shengxuan Huang, Xiang Wu, Bin Chen
Data curation: Shengxuan Huang
Formal analysis: Shengxuan Huang
Funding acquisition: Shengxuan Huang, Xiang Wu, Bin Chen, Shan Qin
Investigation: Shengxuan Huang, Yan Yang
Methodology: Shengxuan Huang, Xiang Wu
Resources: Xiang Wu, Stella Chariton, Vitali B. Prakapenka, Lin Liang, Dongzhou Zhang, Shan Qin
Supervision: Xiang Wu, Bin Chen, Shan Qin
Validation: Shengxuan Huang

Abstract Nitrogen is considered to be transported from Earth′s surface to the top of the lower mantle through subduction. However, little is known on the transportation and fate of subducted nitrogen to the Earth′s interior during slab-mantle interactions. In this study, the stability of subducted sedimentary nitrogen in the reduced mantle was investigated to 35 GPa and 1600 K by laser-heated diamond anvil cell experiments and first-principles calculations. Our results showed that subducted nitrogen-bearing silicates and fluids could not coexist with the metallic iron or iron-rich alloys, and reacted with them to form different products at high pressure-temperature conditions. Combining our results with previous data, we re-determined the relative stability of iron-light element binary compounds to 35 GPa and 1600 K to be Fe-O > Fe-N > Fe-S > Fe-C. This stability sequence contributes to explaining the observation that iron nitrides are trapped as inclusions in sulfur-depleted lower-mantle diamonds and are absent in sulfur-rich ones. The recycling efficiency of subducted sedimentary nitrogen is strongly related to the availability of the metallic iron of the reduced mantle. Hydration of the metallic iron limits the storage of nitrogen in it and contributes to recycling nitrogen to Earth′s surface. Therefore, unlike subducted continental sediments, subducted marine sediments are unlikely to transport a large amount of surficial nitrogen to the metallic iron of the reduced mantle in which nitrogen could reside over long geologic periods.

Plain Language Summary Nitrogen is an essential element for the Earth′s atmosphere and life. A large amount of nitrogen is transported to the Earth′s interior through subduction and may finally reside in the deep Earth. The knowledge on the transportation and storage of nitrogen in the reduced mantle is crucial for our understanding of the Earth′s nitrogen cycle. We combined high-pressure and high-temperature experiments and theoretical calculations to investigate the chemical reactions between subducted nitrogen carriers and metallic iron or iron-rich alloys. The results showed that nitrogen in the subducted silicates and fluids will be extracted to the iron-rich metallic phases when they are relatively excess. Iron nitrides are more stable than sulfides but less stable than oxides at pressure-temperature conditions relevant to the subduction down to 900 km. The incorporation of nitrogen in metallic iron could be an important mechanism to store surficial nitrogen in the reduced mantle. Iron nitrides could be trapped as inclusions in sulfur-depleted lower-mantle diamonds but nitrogen will reside in the metallic melt if superdeep diamonds are formed in a sulfur-rich environment.

1. Introduction

Nitrogen (N) is not only a primary component of the Earth′s atmosphere, but also abundant on the Earth′s surface, reaching several thousand μg/g in continental sediments and several hundred μg/g in marine sediments, respectively (Mysen, 2019). Despite its high concentrations on Earth′s surface and volatile nature, a majority of the Earth′s N is currently believed to reside in the Earth′s deep interior (Johnson & Goldblatt, 2015). The cycling of N between the surface and deep reservoirs is achieved through subduction and volcanic degassing, which play an essential role in modulating the partial pressure (*P*) of atmospheric N and are therefore critical to assess the habitability of our planet (Johnson & Goldblatt, 2015).

A recent study inferred that warm and oxidizing subducted slabs may restrain N from being carried down to the deep mantle (Jackson et al., 2021). However, many lines of evidence from metamorphic belts and from inclusions in superdeep diamonds demonstrated that a large amount of N in slabs might have been conveyed to the

Writing – original draft: Shengxuan Huang
Writing – review & editing: Shengxuan Huang, Xiang Wu, Stella Chariton, Vitali B. Prakapenka, Lin Liang, Dongzhou Zhang, Yan Yang, Bin Chen, Shan Qin

lower upper mantle and even to the bottom of the mantle transition zone (Busigny, Cartigny, Philippot, Ader, & Javoy, 2003; Navon et al., 2017). The net fluxes of N through subduction are affected by the composition of subducted materials, the Earth′s redox state and the secular cooling history of the mantle (Bekaert et al., 2021). Therefore, the investigation on the effect of subduction on the deep N cycle is highly controversial (Barry & Hilton, 2016; Busigny et al., 2011; Labidi et al., 2020). A significant amount of N could be stored in the mantle through subduction instead of being recycled to the surface (Mysen, 2019). Understanding how subducted N resides in the deep mantle provides indispensable clues to assess the effect of subduction on the deep N cycle.

In subducted slabs, a large amount of N is stored in potassium (K) silicates, such as phengite, cymrite and wadeite, in which ammonium cation (NH_4^+) occupies the K^+ site (Sokol et al., 2018; Watenphul et al., 2009). Most of them are stable along the slab geotherm up to the depth of 300 km. They are assumed to decompose into a NH_4^+-bearing hollandite-structured phase and fluids at higher pressures, but limited experimental data are available for the stability of N-bearing silicates above 8 GPa (Chen et al., 2018; Liu et al., 2019). The fluid phase is another significant host for subducted N in the Earth′s upper mantle. The Earth′s redox state controls the speciation of N in slab fluids (Mikhail & Sverjensky, 2014). Under reduced conditions, N exists in the form of NH_4^+, and with increasing oxygen fugacity (f_{O_2}), it is stored predominantly as N_2. N-bearing fluids are believed to upwell to shallow regions, but part of the devolatilized N can be efficiently re-fixed into subducting slabs (Li et al., 2021). Thus far, little is known on the fate of deeply-subducted N hosts during slab-mantle interactions.

The f_{O_2} of the Earth′s interior decreases with depth, and the silicate mantle becomes saturated with the metallic iron (Fe) below 250 km (Rohrbach et al., 2007). N has a good affinity to Fe. The solubility of N in the metallic Fe reaches several weight percent at conditions of the Earth′s upper mantle (Speelmanns et al., 2018), compared to the order of 100 μg/g in major silicates (Li et al., 2013). These results indicate that in the Fe^0-saturated mantle, N released from the slab preferentially partitions into the metallic Fe phase over the silicates. Despite the metallic Fe was proposed to be a potential host for subducted N in the deep mantle (Huang, Wu, et al., 2021; Lv & Liu, 2022), it remains unclear how N is transported from subducted slabs to the metallic Fe of the reduced mantle. It is also unknown whether the volatile-rich metallic Fe is still capable of concentrating N from slabs. On the other hand, N and N-bearing phases are commonly observed in superdeep diamonds. The concentrations of N in them vary considerably from several to thousands of μg/g, which may be associated with the metallic domains in the deep mantle (Kaminsky & Wirth, 2017; Smith et al., 2016). The knowledge of the effect of the metallic Fe on the distribution of N in superdeep diamonds sets additional constraints on the storage of deep N but remains to be explored.

To assess the role of the metallic Fe in the transportation of N from Earth′s surface to the deep interior through slab-mantle interactions, we investigate chemical reactions of N-bearing silicates and fluids with Fe or Fe-rich alloys at high *P* and high temperature (*T*) conditions to 35 GPa and 1600 K using synchrotron radiation X-ray diffraction (XRD) combined with laser-heated diamond anvil cells (LHDAC) and first-principles simulations based on density functional theory (DFT). Our results provide important constraints on the stability of subducted N hosts in the reduced mantle and offer new insights into the heterogeneous distribution of N-bearing inclusions in superdeep diamonds.

2. Methods

2.1. LHDAC Experiments

Natural NH_4^+-bearing phengite samples were extracted from a high-*P* metasediment of the western Alps. Their chemical compositions have been characterized by Busigny, Cartigny, Philippot, and Javoy (2003). The average chemical composition of NH_4^+-bearing phengite is: 55.6 wt. % SiO_2, 0.07 wt. % TiO_2, 21.03 wt. % Al_2O_3, 4.48 wt. % FeO, 0.05 wt. % MnO, 4.42 wt. % MgO, 0.04 wt. % Na_2O, 11.01 wt. % K_2O. The phengite sample contains approximately 0.2 wt% NH_4^+. Other powder samples, including Fe, NH_4Cl and FeS, with a purity >99.9% were purchased from Alfa Aesar.

High pressures were generated using symmetric and short-symmetric DACs with culets of 300 or 400 μm in diameter in six experimental runs. Rhenium gaskets, initially 250 μm thick, were pre-indented into 30∼35 μm thickness. A hole with the diameter of half size of the diamond culet was laser drilled at the center of the indentation and served as the sample chamber. We applied different sample loading arrangements in order to investigate each chemical reaction properly (Figure 1). In runs 1–2, a piece of Fe foil with a thickness of ∼10 μm was

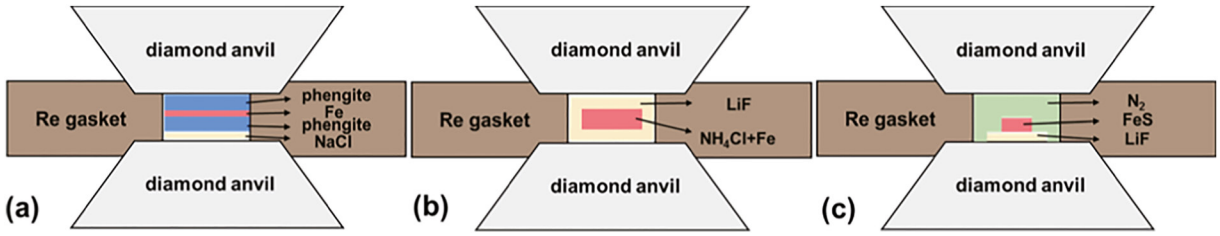

Figure 1. Sample loading arrangements for investigated chemical reactions. (a) for runs 1–2, (b) for runs 3–4 and (c) for runs 5–6.

sandwiched by two phengite plates (~10 μm thickness). In order to accurately determine the internal *P*, a NaCl plate (~5 μm thickness) was placed between the reagent and the anvil (Dorogokupets & Dewaele, 2007). In runs 3–4, NH_4Cl and Fe powders were mixed at a molar ratio of 1:1 and compressed into plates with a thickness of ~15 μm. The mixture was then sandwiched by two LiF plates, which acted as a thermal insulator, a *P* calibrator and as a *P*-transmitting medium (PTM) (Liu, Dubrovinsky, et al., 2007). In runs 5–6, a piece of FeS foil was placed on a LiF plate. The DACs were loaded with nitrogen liquid, which served as a reactant and a PTM.

Synchrotron XRD experiments were carried out at beamline 13-IDD and 13-BMC, Advanced Photon Source (APS), Argonne National Laboratory (ANL), at beamline 15U of Shanghai Synchrotron Radiation Facility (SSRF), and at beamline 4W2 of Beijing Synchrotron Radiation Facility (BSRF). Experimental details, including the incident X-ray wavelength and beam size, were summarized in Table S1 of the Supporting Information S1. In runs 1–2, the sample was heated from both sides at a given *P* using a double-sided laser heating system with the flat-top heating spot size of ~10 μm in diameter (Prakapenka et al., 2008). The XRD data were collected before, during and after heating. In runs 3–6, high *T* annealing was employed using a portable laser heating system installed at School of Earth and Space Sciences, Peking University. Note that the heating process lasted for more than 30 min in these runs in order to achieve the equilibrium for each chemical reaction. DACs were then taken to the beamline to acquire XRD data at room *T*. The XRD spectra were integrated and processed using Dioptas and GSAS + EXPGUI software, respectively. The lattice parameters were refined using model-biased Le Bail method.

2.2. First-Principles Calculations

DFT-based first-principles simulations were performed using the Vienna *ab-initio* simulation package (Kresse & Joubert, 1999). The exchange correlation potential was treated by GGA-PBE pseudopotential (Perdew et al., 1996), which was shown to yield good results for Fe alloys (Mookherjee et al., 2011). The energy cut-off was set to 1000 eV in all static calculations. The energy convergence criterion for electronic self-consistent calculations was 10^{-6} eV. The *k*-points grids were set according to the lattice parameters of each candidate structure. The spin-polarization of Fe was included in our calculations. The ferromagnetic, antiferromagnetic and nonmagnetic states were considered for selected structures. In addition, a DFT + *U* method was introduced to correctly describe the strong correlation effect (Dudarev et al., 1998). The on-site Coulomb interaction parameter $U = 3$ eV and the Hund coupling constant $J = 1$ eV were applied into Fe in GGA + *U* calculations (Huang et al., 2018). The lattice parameters, atomic positions and individual magnetic moments were allowed to relax at each given volume (*V*) to obtain the minimum total energy (*E*). The *V*-*E* data of each candidate phase were fitted by the third-order Birch-Murnaghan (B-M) equation of state (EoS). The relative enthalpy of the phase assemblage was used to examine whether the target chemical reaction was energetically favorable.

3. Results

3.1. Reactions Between NH_4^+-Bearing Phengite and Fe

In run-1, starting materials were compressed to ~8 GPa at room *T*. The XRD pattern displayed that phengite did not undergo any structural transition and coexisted with Fe under such conditions (Figure S1a in the Supporting Information S1). Heating the sample assemblage to 1150 ± 50 K led to the emergence of a few new reflections (Figure 2). As *T* increased, the intensities of new peaks became significant and those of starting materials weakened. These results indicated that phengite reacted with Fe at high *P*-*T* conditions. In run-2, the sample

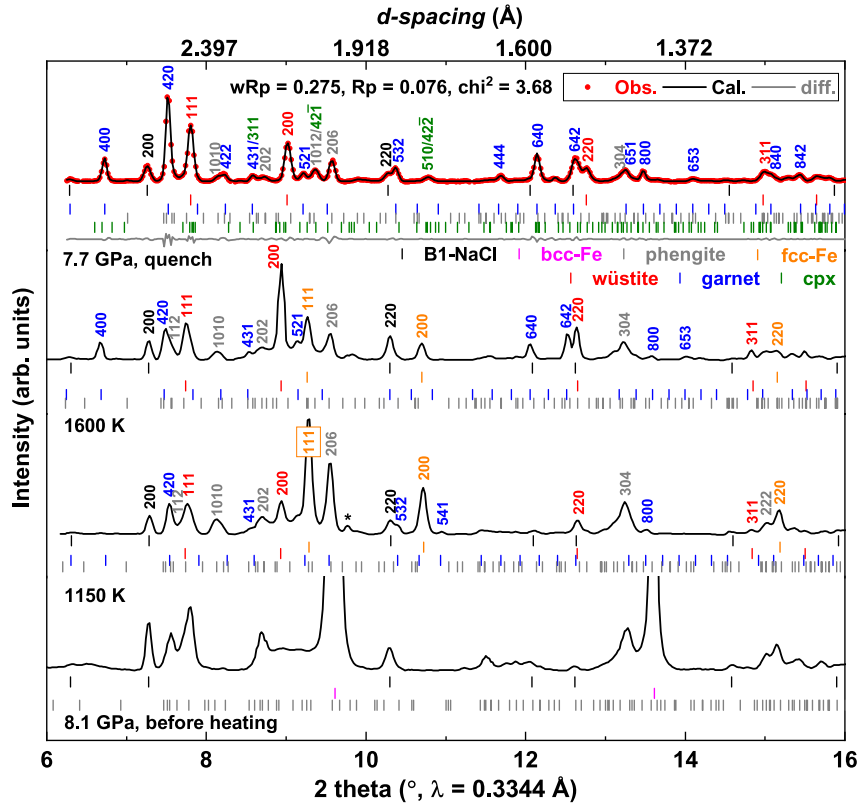

Figure 2. Representative measured XRD patterns of chemical reactions between NH_4^+-phengite and Fe at 8.1 GPa before, during and after heating in run-1. Le Bail refinements (red dotted curves) were carried out after background subtraction. Black, pink, orange, red, blue, green and gray ticks represent Bragg peaks of NaCl, *bcc*-Fe, *fcc*-Fe, wüstite (FeO), garnet, clinopyroxene and phengite, respectively. The *hkl* index of the assigned phase for each Bragg peak is listed. The stars represent unassigned reflections.

assemblage was laser-heated gradually from 1200 ± 50 K to 1500 ± 50 K at ~13 GPa. Again, new reflections became dominant with increasing *T*, suggesting phengite reacted with Fe (Figure 3). The sample assemblage was further heated for more than ten minutes at the highest *T* (i.e., 1600 K in run1 and 1500 K in run2) to achieve the equilibrium for the target system in both runs.

The model-biased Le Bail fitting was performed to analyze the XRD patterns collected at high *P*-*T* conditions and after quenching (Figures 2–3 and Figures S2–S3 in the Supporting Information S1). The fitting results indicate that our models are reasonable. It is to be noted that the fitting residue resulted mainly from the small mismatch of phengite. In runs 1–2, a piece of Fe foil was sandwiched by two phengite plates (Figure 1a). Phengite might suffer a large deviatoric stress and *T* gradient in such sample assemblage configuration causing the mismatch.

In run-1, the majority of new Bragg peaks could be assigned to wüstite (FeO) and garnet and the remaining new peaks were assigned to clinopyroxene (Figure 2 and Figure S2 in the Supporting Information S1). The fitted unit-cell volumes were 77.09(3) Å^3 for wüstite, 1482.3(4) Å^3 for garnet, and 401.9(2) Å^3 (a = 9.473(3) Å, b = 8.651(5) Å, c = 5.102(3) Å, and β = 105.99(4)°) for clinopyroxene at 7.7 GPa after quenching. In contrast, garnet was absent during heating to 1500 ± 50 K at ~13 GPa. The products were composed dominantly of wüstite and clinopyroxene in run-2 (Figure 3 and Figure S3 in the Supporting Information S1). The fitted unit-cell volumes were 76.57(2) Å^3 for wüstite, and 392.5(1) Å^3 (a = 9.402(1) Å, b = 8.579(1) Å, c = 5.062(1) Å, and β = 106.01(1)°) for clinopyroxene at 12.3 GPa after quenching. These parameters were comparable to previous results (Figure S4 in the Supporting Information S1). For instance, the difference in the V of wüstite between our data and those of Fischer et al. (2011) was less than 1%. The unit-cell volumes of garnet or clinopyroxene obtained in this study were both larger than their Mg-endmembers, and close to (Fe, Ca, Na)-bearing phases (Xu et al., 2019). Either garnet and clinopyroxene can form complex solid solutions. The compositional variation also affects their unit-cell volumes. Considering the composition of phengite used here, we suppose that an amount of

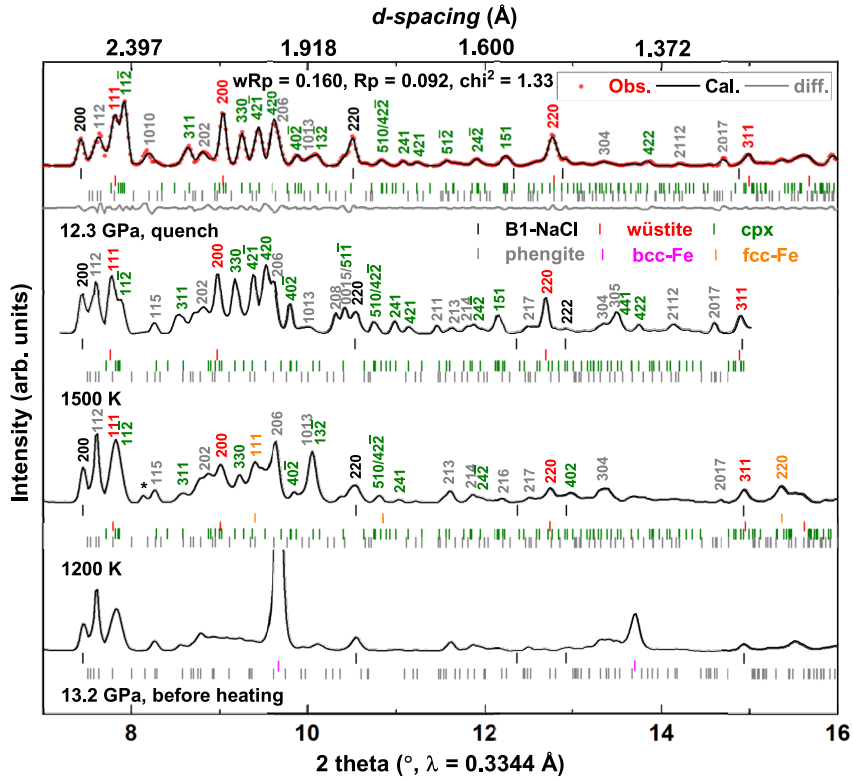

Figure 3. Representative measured XRD patterns of chemical reactions between NH_4^+-phengite and Fe at 13.2 GPa before, during and after heating in run-2. Le Bail refinements (red dotted curves) were carried out after background subtraction. Black, pink, orange, red, green and gray ticks represent Bragg peaks of NaCl, *bcc*-Fe, *fcc*-Fe, wüstite (FeO), clinopyroxene and phengite, respectively. The *hkl* index of the assigned phase for each Bragg peak is listed. The stars represent unassigned reflections.

Fe and K should be incorporated into garnet and clinopyroxene. Indeed, we did not observe any other K-bearing crystalline phases in the products in both runs. The K-bearing component could be also dissolved into fluids during heating. We observed a diffused background in the integrated XRD patterns at high *P*-*T* conditions, implying the existence of a small portion of melt under such consitions (Figure S5 in the Supporting Information S1). However, the diffused background could not be clearly identified in the quenched XRD patterns. The fluids might diffuse into unheated areas during heating and was thus not recorded in the quenched XRD patterns. The reaction of Fe with the structural water of phengite was responsible for the formation of wüstite in runs 1–2. Zhu et al. (2019) reported that hydrous wadsleyite could react with Fe to form wüstite, which was further dissolved into Fe-free wadsleyite or ringwoodite at mantle transition zone conditions. Our results were consistent with their observations. In terms of N, Fe nitrides were not observed. N might not bond with Fe since Fe was nearly exhausted in runs 1–2. N was likely to be incorporated into silicate products or fluids. To briefly summarize, when Fe was relatively deficient, NH_4^+-bearing phengite reacted with Fe to form mainly wüstite, silicates (garnet or clinopyroxene) and fluids at pressures of 8∼13 GPa and at temperatures of 1150∼1600 K.

3.2. Reactions Between NH_4Cl and Fe

In run-3, after heating the mixture of NH_4Cl and Fe to 1200 ± 200 K at ∼10 GPa for ∼30 min, a few new Bragg reflections emerged, implying the occurrence of the reaction between starting materials under such conditions (Figure 4a). The dominant reflections in the XRD pattern did not change significantly and some of the weak peaks disappeared when the sample assemblage was decompressed to the ambient *P*. In run-4, starting materials were compressed to ∼26 GPa and then heated to 1500 ± 200 K for ∼30 min. Similarly, Fe reacted with NH_4Cl and was exhausted during high *P*-*T* treatment (Figure 4b). The majority of Bragg reflections from the products remained to ∼10 GPa. Some of them disappeared below ∼10 GPa, suggesting that some of the products were quenchable at relatively low pressures.

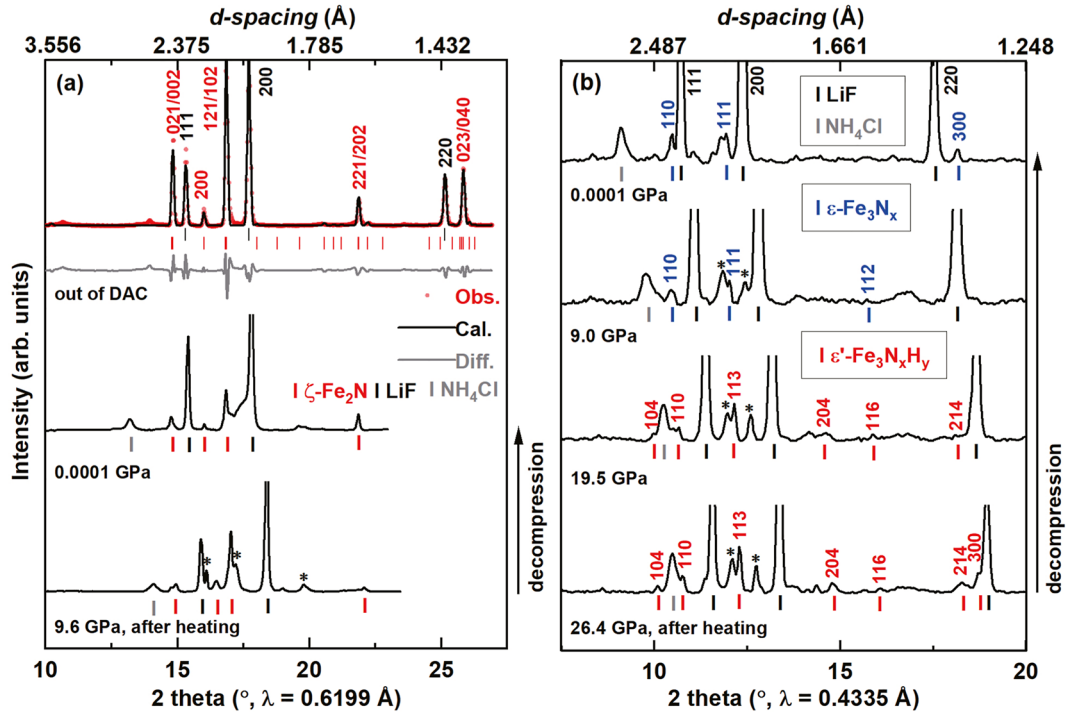

Figure 4. Representative measured XRD patterns of chemical reactions between NH_4Cl and Fe after heating under high P in run-3 (a) and run-4 (b). Le Bail refinements (red dotted curves) were carried out after background subtraction. The Bragg peaks of ζ-type Fe_2N, ε-type $Fe_3N_{1.10(2)}$ and ε'-type $Fe_3N_{1.10(2)}H_{0.72(9)}$ phases are marked. The stars represent unassigned reflections.

In run-3, the orthorhombic ζ-type Fe_2N (space group: *Pbcn*) was identified as one major product after laser annealing (Figure 4a). Sharp diffraction spots with d-spacings of 3.484 Å and 2.825 Å were assigned to 110 and 111 peaks of ζ-type Fe_2N, respectively, whereas they were not allowed for ε-type Fe_3N_x (space group: $P3_12$) (Figure S1b in the Supporting Information S1). Thus, we assigned this phase to ζ-type Fe_2N instead of ε-type Fe_3N_x. In run-4, as shown in Figure 4b, seven diffraction peaks identified from the quenched XRD pattern could be indexed by a trigonal structure with lattice parameters $a = 4.620(2)$ Å, $c = 12.57(1)$ Å and $V = 232.4(2)$ Å^3 at 26.4 GPa and 300 K (Table S2 in the Supporting Information S1). The reflections with $l = 4$ of this new phase (denoted as ε'-type) disappeared below ~10 GPa. The remaining peaks could be assigned to a trigonal ε-type structure with lattice parameters $a = 4.718(4)$ Å, $c = 4.292(12)$ Å and $V = 82.75(20)$ Å^3 at 8.4 GPa and 300 K (Figure 4b). The a-axis parameter of the ε'-type phase was similar to that of ε-type Fe_3N_x, while the c-axis was approximately three times longer than that of the ε-type phase. We speculated that the crystal structure of the ε'-type phase could be similar to that of the ε-type phase. The ε'-type unit-cell seems to be three ε-type unit-cells stacked along the c-axis. The crystal structure could not be resolved in our study because of the limited opening angle of the DAC. It is to be noted that the ε'-type phase was not observed in the Fe-N binary system (Minobe et al., 2015). This suggested that a third element, such as hydrogen (H), could have been incorporated in ε-type Fe_3N_x, which will be discussed in detail in the next section.

In addition to Fe nitrides, there were other new peaks in T-quenched XRD patterns. They could not be assigned to one or several phases using the existing structural data, such as $FeCl_2$, $FeCl_3$, HCl and FeH_x. They might belong to the unknown high-P forms of these binary compounds or to the structures of novel compounds containing more than two elements. In run-3, we also measured the XRD pattern of the recovered sample at ambient conditions where the sample assemblage (still sandwiched by LiF layers) had been taken out of the DAC for six months. The reflections of ζ-type Fe_2N were clearly observed with high intensities. In contrast, two new Bragg peaks located at 2θ of 16.12° and 17.22° disappeared, indicating that some of products were volatile or metastable (Figure 4a). The reaction between Fe and NH_4Cl might be simplified to that between Fe and NH_3. The reaction of Fe with NH_3 at high P-T conditions could be described as $2xNH_3 + 6Fe \rightarrow 2Fe_3N_x + 3xH_2$.

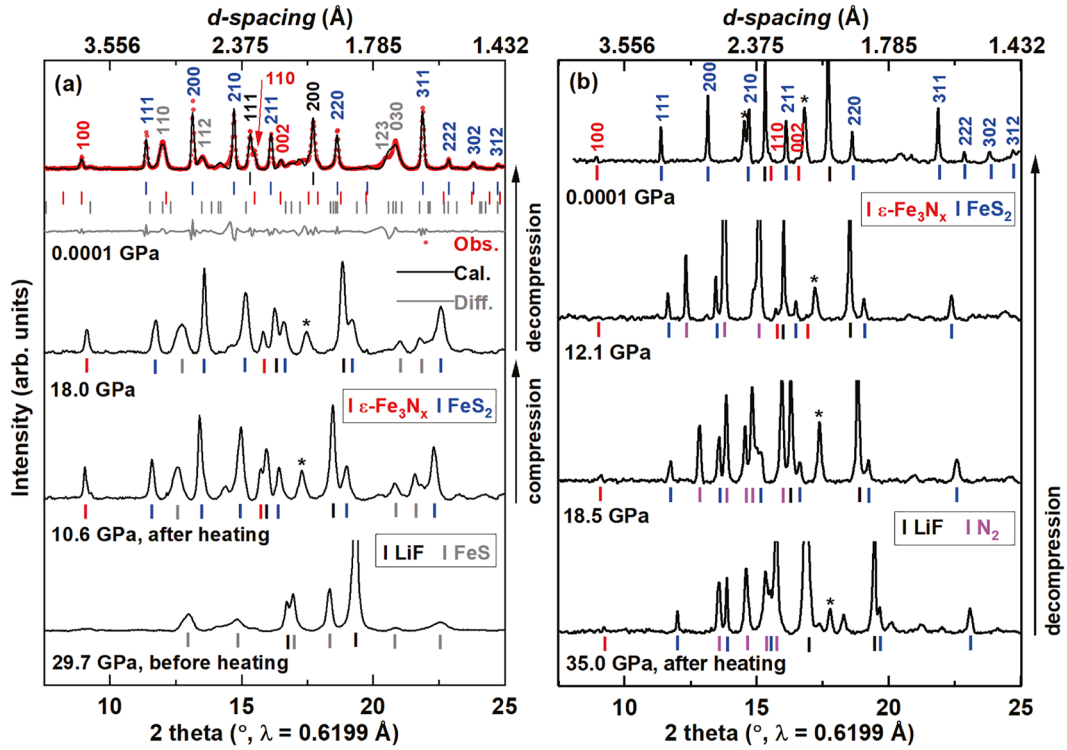

Figure 5. Representative measured XRD patterns of chemical reactions between N_2 and FeS under high *P* before and after heating in run-5 (a) and run-6 (b). Le Bail refinements (red dotted curves) were carried out after background subtraction. The black, gray, pink, red and blue ticks represent Bragg peaks of LiF, FeS, N_2, ε-type $Fe_3N_{0.6}$ and FeS_2, respectively. The stars represent unassigned reflections.

3.3. Reactions Between N_2 and FeS

In run-5, N_2 and FeS were first compressed to ~30 GPa at room *T*. The XRD pattern showed the presence of the high-*P* monoclinic FeS phase and LiF (Figure 5a). The peaks of N_2 were too weak to be observed in the integrated XRD pattern at 29.7 GPa. Heating the sample assemblage at 1500 ± 200 K for a few minutes caused the sample chamber to shrink likely due to the consumption of N_2. The sample assemblage was further heated for more than 15 min after the sample chamber became stable. The *P* inside the DAC decreased to 10.6 GPa after annealing. The XRD pattern after quenching was significantly different from that before heating, indicating that FeS reacted with N_2 at high *P-T* conditions (Figure 5a). In run-6, starting materials containing excess N_2 were laser-heated to 1500 ± 200 K for ~30 min at ~35 GPa (Figure 5b). The *P* inside the DAC remained nearly unchanged after heating in run-6. Figure S6 in the Supporting Information S1 demonstrated that the products obtained in run-6 were similar to those in run-5.

The refinement of XRD data suggested that the recovered sample should contain mainly pyrite (FeS_2) and ε-type Fe_3N_x (Figure 5a). The chemical reaction between FeS and N_2 at high *P-T* conditions could be described as $xN_2 + 12FeS \rightarrow 6FeS_2 + 2Fe_3N_x$. DFT-based first-principles calculations were performed to investigate the chemical reaction between FeS and N_2 (Table S3 in the Supporting Information S1). Theoretical simulations showed that the assemblage of FeS_2 and Fe_3N had a lower enthalpy than that of FeS and N_2 above 12 GPa, favoring the reaction (Figure S7a in the Supporting Information S1). The refined volumes of FeS_2 were plotted as a function of *P* (Figure S7b in the Supporting Information S1). The *P-V* data of FeS_2 were fitted using the second-order B-M EoS, yielding $V_0 = 159.06$ Å^3 and $K_0 = 159.7$ GPa. They were in good agreement with those of our recent study on endmember FeS_2 (Huang et al., 2018). The results implied that FeS_2 consisted of primarily Fe and sulfur (S) without incorporating N in its structure. The unit-cell volumes of ε-type Fe_3N_x at ambient conditions were refined to be 79.32(4) Å^3 in run-5 and 79.02(1) Å^3 in run-6, respectively. The *x* value in ε-type Fe_3N_x was estimated to be ~0.6 (Litasov et al., 2017). This value was close to the lower limit ($x = 0.5$) for ε-type Fe_3N_x, indicating that

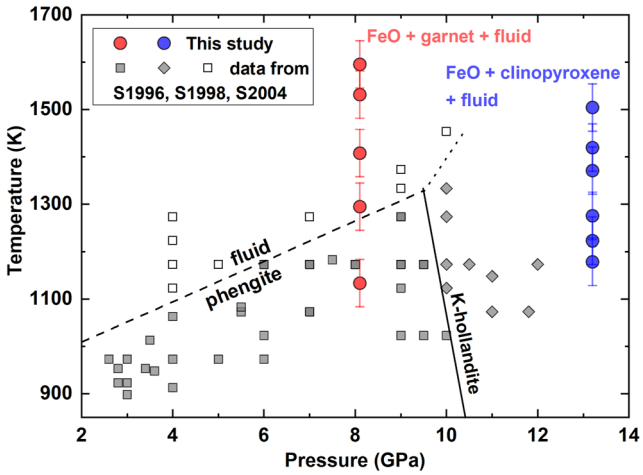

Figure 6. Phase diagram of phengite at high *P-T* conditions. The squares and diamonds display the experimentally determined stability field of NH_4^+-free phengite in previous studies (Schmidt, 1996; Schmidt et al., 2004; Schmidt & Poli, 1998). The circles represent our experimental data. The red and blue marks represent the different products of the chemical reaction between phengite and Fe at 8.1 GPa and 13.2 GPa, respectively.

Fe_3N_x did not contain S. Therefore, there was no apparent evidence of forming Fe-N-S ternary compounds in our experiments. N extracted Fe from FeS and kept N and S separate below solidus.

4. Discussion

4.1. Stability of NH_4^+-Bearing Phengite

Pressure is shown to enhance the thermal stability of phengite as demonstrated in literature experimental data on the stability of NH_4^+-free phengite in systems with various bulk compositions (Figure 6) (Schmidt, 1996; Schmidt et al., 2004; Schmidt & Poli, 1998). The breakdown *T* of phengite increases from ~1000 K at 2 GPa to ~1300 K at 9 GPa. Furthermore, phengite decomposes to form K-hollandite at ~10 GPa. In terms of the NH_4^+-bearing counterpart, few experiments have been conducted at simultaneously high *P-T* conditions. Two synthetic experiments confirmed that it was stable at 1000 K and 4 GPa or 1300 K and 6.3 GPa (Sokol et al., 2018; Watenphul et al., 2009). Raman and IR spectroscopic measurements on phengite demonstrated that NH_4^+ substitution hindered H transition and delayed softening of the lattice of phengite at high *P-T* conditions (Huang, Yang, et al., 2021). They implied that the incorporation of NH_4^+ even enhanced the thermal stability of phengite at pressures below 10 GPa. The dehydration *T* of NH_4^+-bearing phengite at high *P* may be similar to that of the NH_4^+-free analog, while the NH_4^+ component has a negligible effect on the stability of the high-*P* hollandite-structured phase.

Our experiments have demonstrated that phengite reacts with Fe at 8 GPa and 1150 K, at which phengite should be stable in the absence of Fe (Figure 6). One of the main products of this reaction is FeO, which is absent in the product assemblage of phengite dehydration. Kyanite is not observed in the products. FeO can further react with kyanite, which will be subsequently dissolved in garnet or clinopyroxene (Schmidt et al., 2004). Furthermore, phengite reacts with Fe to form mainly FeO and clinopyroxene at 13 GPa and 1200 K (Figure 6). Heating the single phengite phase at 12 GPa and 1200 K resulted in the formation of garnet, K-hollandite, kyanite and fluids (Chen et al., 2018). K-hollandite and kyanite are incompatible with FeO and react with it to form clinopyroxene (Schmidt et al., 2004). Therefore, we conclude that the reaction between Fe and structural water of phengite triggers its dissociation prior to dehydration or structural transformation, and the resulting FeO considerably affects the phase assemblage of the products.

Fe nitride phases are not detected as products in the reaction between Fe and NH_4^+-bearing phengite. Our subsequent experiments confirm that Fe could react with the NH_4^+-dominant phase (NH_4Cl) to form Fe nitrides at high *P-T* conditions. The natural phengite sample used in our study contains ~0.2 wt% ammonium, much lower than that of NH_4Cl. The chemical reactivity of NH_4^+, as a dilute component in phengite, should be significantly low. However, Zhu et al. (2019) have found that Fe could react with hydrous wadsleyite with ~0.9 wt% water to form wüstite and nearly anhydrous silicates, similar to the reaction between Fe and pure H_2O. This might be applied in our study since both N and O could form a strong bond with Fe and the concentration of NH_4^+ in phengite is comparable to that of water in hydrous wadsleyite. We argue that the reaction between Fe and NH_4^+ is anticipated to occur in the Fe-phengite system if Fe is excess in runs 1–2.

4.2. Hydrogen in Fe Nitrides

The unit-cell volumes of ζ-type, ε-type and ε′-type phases obtained in runs 3–4 were plotted as a function of *P* (Figure 7a). At ~10 GPa, the *V* of the ζ-type phase synthesized in run-3 is 2.8% larger than that of pure ζ-type Fe_2N (Schwarz et al., 2009). In contrast, it is close to that of pure ζ-type Fe_2N when *P* is fully released. In terms of the ε′-type phase, its compressive behavior (solid red curve in Figure 7a) generally follows the compression curve of pure ε-type Fe_3N_x (dashed blue curve in Figure 7a) in the *P* range of 15~25 GPa (Litasov et al., 2017). Below 10 GPa, we observed an anomaly in *V* evolution accompanied by the ε′-to-ε transition. We attribute the *V* expansion and anomalous *V* evolution to the incorporation of H in Fe nitrides. Previous studies have found that

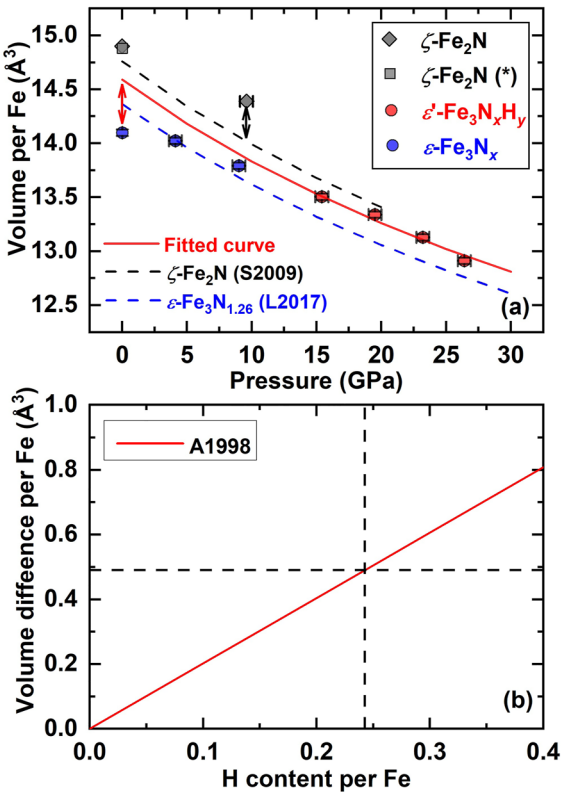

Figure 7. (a) Evolution of unit-cell volumes of ζ-type, ε-type and ε'-type phases as a function of P. Previous experimental data of ζ-type and ε-type Fe nitrides are plotted for comparison (Litasov et al., 2017; Schwarz et al., 2009). The gray square represents the data point collected after the sample assemblage (still sandwiched by LiF layers) was taken out of the DAC for six months. (b) Evolution of V expansion of Fe as a function of H content (Antonov et al., 1998). The horizontal and vertical dashed lines represent the V difference and the correspondingly derived H concentration obtained in run-4, respectively.

Fe and Fe-rich alloys can incorporate a significant amount of H under high P (Antonov et al., 1998; Tagawa et al., 2016). In their studies, the H insertion enlarges the V of the H-free counterpart depending on the H content, and the H-bearing phase cannot be quenched to the ambient P and at room T. Our experimental observations are consistent with previous results.

To estimate N and H contents of $Fe_3N_xH_y$ obtained in run-4, we follow the methods implemented by Litasov et al. (2017) and Tagawa et al. (2016), respectively (Figure 7a). First, H is assumed to fully escape from the ε-type phase at ambient P. The N concentration can be calculated through the linear relation of V versus x established by Litasov et al. (2017). This linear relation provides a relatively accurate estimation on the N content in ε-type Fe nitrides. The V of ε-type Fe_3N_x at ambient P (denoted as V_0) is 14.10(3) Å^3 per Fe, which yields $x = 1.10(2)$. Second, the V-P data of ε'-type $Fe_3N_xH_y$ are fitted to the B-M EoS to obtain the V at ambient P (denoted as V_0'). Due to limited data, we fix K_0 and K_0' as 163 GPa and 5.3, respectively (Litasov et al., 2017), and obtain V_0' to be 14.59(2) Å^3. Third, the difference between V_0 and V_0' is assumed to be caused by H incorporation. Previous in situ neutron diffraction experiments show that the V of *hcp*-Fe can expand by 2.02 Å^3 if one H atom enters the interstitial vacancy of the host metal (denoted as V_H) (Antonov et al., 1998). The H concentration can be estimated by the equation $y = 3(V_0' - V_0)/V_H$ (Figure 7b). The derived y value is 0.72(9). Therefore, the composition of $Fe_3N_xH_y$ is determined as $Fe_3N_{1.10(2)}H_{0.72(9)}$. Note that we do not estimate the H content of the ζ-type phase obtained in run-3 due to the lack of V data upon decompression.

The ε-type structure is derived from a distorted hexagonal close-packed (*hcp*) structure of Fe. N and H atoms may occupy the octahedral sites (Litasov et al., 2017; Tagawa et al., 2016). The number of octahedral sites in the *hcp* structure is equivalent to that of Fe atoms. Due to strong Coulomb repulsions between octahedra with increasing N contents in the ε-type structure, only half of octahedral sites can be occupied by N atoms, $x_{max} = 1.5$. H atom is much smaller than N atom. The repulsion of the octahedron centered by H atom with the neighbor octahedron is less pronounced in comparison with that between octahedra both centered by N atoms. Therefore, there are many unoccupied octahedral sites for H in ε-type Fe_3N_x.

In addition to enlarging the unit-cell V, the insertion of H in a Fe alloy may also affect its crystal structure. For instance, previous experiments have found that the incorporation of H in FeS leads to the formation of the novel FeSH compound with a totally different structure from FeS (Piet et al., 2021). At this moment, we can only provide lattice parameters of ε'-type $Fe_3N_xH_y$ but its crystal structure cannot be resolved. We speculate that H might occupy the octahedral vacancies in an ordered way since H incorporation leads to a ε-to-ε' transition. Further in situ neutron diffraction measurements can help to determine the occupation of H in Fe nitrides and to reveal the formation mechanism of ε'-type $Fe_3N_xH_y$.

4.3. Relative Stability of Fe-Light Element Compounds Under High *P*

According to our experimental and theoretical results, we built provisional phase diagrams for the Fe-N-H and Fe-N-S systems (Figure 8). Fe and NH_3 are incompatible and react to form a more stable phase assemblage at pressures of 10~25 GPa and at temperatures of 1200~1500 K. Above a certain P, Fe nitrides are capable of incorporating H to form a Fe-N-H ternary compound with a new structure, which should complicate the subsolidus phase relation of the Fe-N-H system (solid red line in Figure 8a). It is found that Fe prefers to bond with carbon (C) instead of H below 1700 K at pressures of 10~70 GPa, and this relation reverses at higher temperatures (Lai et al., 2022; Narygina et al., 2011). It remains an open question whether H will have a better affinity to Fe than N at higher P-T conditions, which will lead to a new reaction $6Fe + 2NH_3 \rightarrow 6FeH + N_2$ (soli blue line in Figure 8a). Moreover, Fe nitrides transform or decompose into Fe_7C_3-type Fe_7N_3 above 40 GPa (Minobe et al., 2015). The

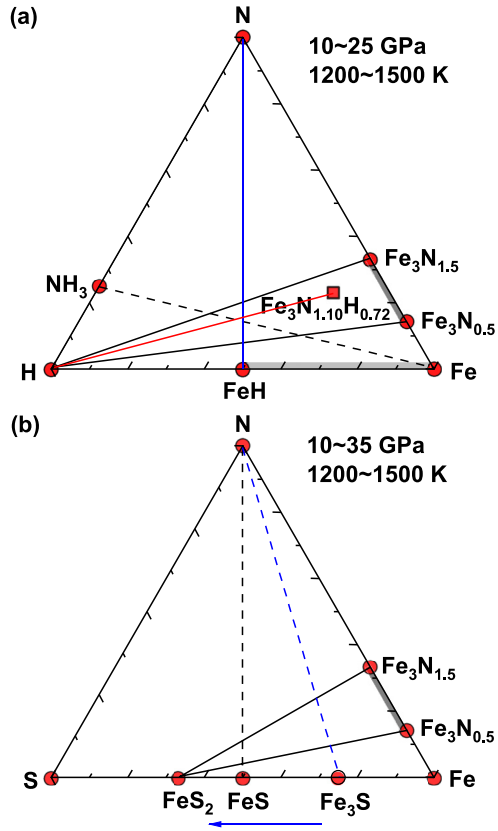

Figure 8. Provisional phase diagrams of (a) Fe-N-H and (b) Fe-N-S ternary systems. The dashed and solid lines connect the reagents and products, respectively. The compositional ranges of Fe_3N_x and FeH_x are shown as gray bars. The solid blue line connects the speculated products of the reaction between NH_3 and Fe at higher temperatures.

formation of Fe_7N_3 may further alter the phase diagram of the Fe-N-H system above 40 GPa. In terms of the Fe-N-S system, FeS is unstable in the presence of N_2 and decomposes into FeS_2 at pressures of 10∼35 GPa and at temperatures of 1200∼1500 K. Multi-anvil press experiments have shown that at conditions of 6∼20 GPa and 700∼1500 K, Fe_3C is nitrogenerated to form ε-type Fe_3N_x, whereas FeS is stable (Litasov et al., 2016). N_2 is the N resource in the present study, whereas CH_2N_4 was used in previous experiments. CH_2N_4 decomposes into NH_3, N_2 and C (graphite and diamond) at high *P-T* conditions. The excess solid phases of C can deposit on the surface of FeS powder, which may significantly decrease the reaction efficiency. In our experiments, the FeS foil is immersed in N_2 and they can react with each other sufficiently during laser heating. In addition, various Fe-rich sulfides are stable above 10 GPa, such as Fe_3S, Fe_2S and Fe_3S_2, which can be considered as the assemblage of "mFe·nFeS" (Fei et al., 1997, 2000). It is anticipated that these Fe-rich sulfides are also unstable when the system contains N_2 at high *P-T* conditions. N will extract Fe from these compounds resulting in the formation of FeS_2, the most S-rich compound in the Fe-S system so far. However, this prediction may not be valid if Fe-N-S ternary compounds could form at higher *P-T* conditions. Combining our results with previous data, we modify the stability sequence of Fe-light element (LE) binary compounds to be Fe-O > Fe-N > Fe-S > Fe-C at pressures to 35 GPa and at temperatures to 1600 K.

The present data show that H diffuses into Fe nitride and expands its unit-cell *V* under high *P*. Similar phenomena are also observed in other Fe alloys, such as FeS (Shibazaki et al., 2011), *hcp*-$Fe_{0.88}Si_{0.12}$ (Tagawa et al., 2016), and *hcp*-$Fe_{0.94}C_{0.06}$ (Lai et al., 2022). H only diffuses into the octahedral vacancy of these compounds without changing their structures. In contrast, there is no experimental evidence of the incorporation of H into Fe_3C (Litasov et al., 2016). It is likely due to the fact that there are no octahedral vacancies in Fe_3C. Therefore, the reaction between Fe and excess C-H compounds at pressures of 10∼70 GPa and relatively low *T* produces Fe_3C and H_2 rather than Fe_3CH_x (Lai et al., 2022; Litasov et al., 2016; Narygina et al., 2011). In such case, the diffusion of H into the host alloys may not necessarily indicate that the stability of Fe-H can be equal to the host binary compounds (i.e., Fe-N and Fe-S). On the other hand, our results further demonstrate that a Fe-N-H ternary compound with a new structure can be formed above a certain *P*. Piet et al. (2021) also observe a FeSH compound with a structure different from FeS or FeH at pressures above 35 GPa. These observations imply that Fe hydrides are compatible with Fe nitrides and sulfides at higher pressures. The bulk compositions of the starting materials can affect the specific reaction products of the ternary Fe-LE systems. But they cannot change the stability sequence of Fe-LE binary compounds. Whereas the formation of new ternary compounds reflects the alteration of the relative stability of Fe-LEs. Because the stability field of ε'-type $Fe_3N_xH_y$ is not well constrained in this study, the Fe-H system is not included in the stability sequence.

5. Implications

5.1. Implications for Subducted Continental Sedimentary N

The geochemical and petrological evidence indicates that continental sediments can be recycled to the Earth′s mantle transition zone (Liu, Zhang, et al., 2007). Mineral physics data also provide important clues that continental crusts are possible to be subducted to 300∼550 km depth (Hao et al., 2020). Because subducted continental sediments are likely to suffer a relatively cold subduction geotherm (Zheng & Chen, 2016), N-bearing silicates in them could be stable to the Earth′s mantle transition zone against decomposition or melting during subduction (Massonne & Fockenberg, 2022; Watenphul et al., 2009). Subducted continental sediments contain thousands of μg/g N on average (Mysen, 2019). Despite that they are only a thin layer of the subducted slab, 2×10^{19} moles of N in them might have been transported to the Earth′s interior through geologic times (Barry & Hilton, 2016).

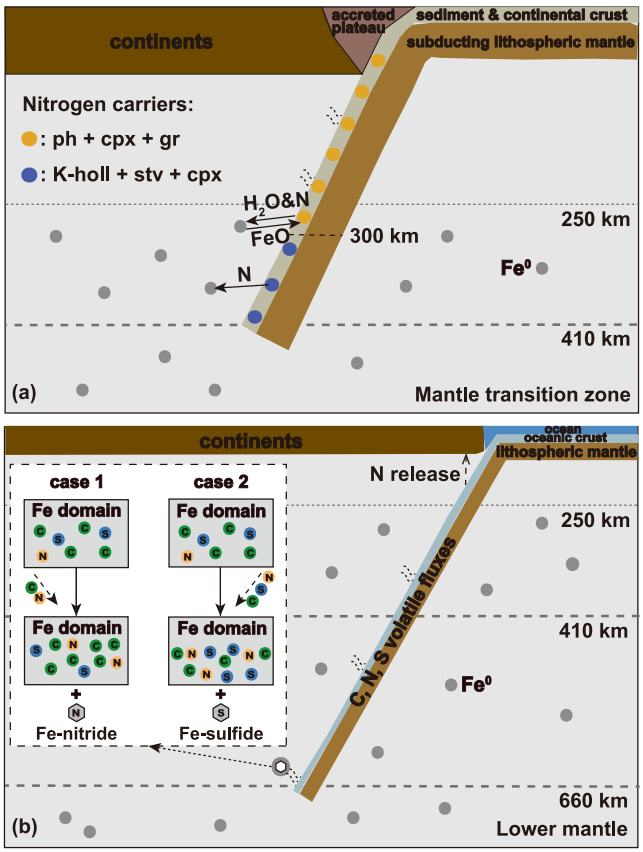

Figure 9. Schematic models for transportation of continental sedimentary/ continental crust N (a) and marine sedimentary/ oceanic crust N (b) to the reduced mantle during slab-mantle interactions. Phen, cpx, gr, K-holl and stv represent phengite, clinopyroxene, garnet, K-hollandite and stishovite, respectively. (a) In continental sediments and continental crusts, N is stored in phengite, clinopyroxene and garnet above ~300 km, and in K-hollandite, stishovite and clinopyroxene below ~300 km. At depth greater than 250 km, the metallic Fe could react with N-bearing silicates or fluids transporting N from subducted slabs to the reduced mantle. In contrast, the reactions of structural or free water with Fe limit the storage of N in metallic Fe. (b) Superdeep diamonds could form through the reactions between subducted carbonates and Fe in the reduced mantle. The stability sequence of Fe-N > Fe-S > Fe-C contributes to the heterogeneous distribution of Fe nitride phases in superdeep diamonds as reported by Kaminsky and Wirth (2017) and by Smith et al. (2016).

The subducted sediments consist of ~20 vol% phengite, ~30 vol% coesite, ~40 vol% clinopyroxene and ~10 vol% garnet at depth above 300 km, and are composed primarily of K-hollandite, stishovite, clinopyroxene and garnet in deeper regions (Wu et al., 2009). In such phase assemblages, N resides predominantly in K-bearing silicates (phengite and K-hollandite) and secondarily in K-free phases (stishovite and clinopyroxene) (Fukuyama et al., 2020; Li et al., 2013; Mysen, 2019).

Below 250 km, the metallic Fe is involved in slab-mantle interactions. Our results have demonstrated that phengite, the major host of N in subducted slabs above 300 km, reacts with Fe to form FeO and garnet/clinopyroxene. And the K-hollandite phase formed from phengite below 300 km cannot coexist with Fe. N hosted in these compounds will be incorporated into other phases. In the natural system, the concentration of N is likely to be hundreds to thousands of μg/g in phengite and could be at the wt% level in subducted fluids (Mysen, 2019). As we have discussed in the former section, N with a concentration of several thousand μg/g in its silicate hosts is able to bond with metallic Fe when Fe is relatively excess. Note that pure NH_4Cl and N_2 samples used in our study cannot directly reflect the realistic composition of the subducted N-bearing fluid. However, the reaction between Fe and NH_4^+/N_2 in the fluid can also occur, because the N concentration in the subducted fluids could be much higher than that in silicates. In addition, provided a large partition coefficient of N between Fe and stishovite or between Fe and clinopyroxene, N is likely to be transported to the metallic phase when two phases are in equilibrium (Fukuyama et al., 2020; Li et al., 2013). Therefore, the metallic Fe of the reduced mantle is capable of reacting with major N hosts in slabs and alloying with N during slab-mantle interactions (Figure 9a). The incorporation of N in metallic Fe could be an important mechanism to store surficial N in the reduced mantle.

However, a key issue that should be also considered is the reaction sequence. Specifically, the following two cases are presented.

1. If N-bearing silicates or fluids are excess in comparison with Fe, only a portion of them will react with Fe to form FeO, garnet/clinopyroxene and fluids. Because Fe oxides are more stable than nitrides at conditions of the Earth′s mantle, the interaction of structural or free water with Fe hinders N to bond with Fe and limits the storage of N in metallic Fe (Figure 9a). The solubility of N in garnet or clinopyroxene is only tens of μg/g (Li et al., 2013). Part of N can be stored in stishovite, which is able to incorporate up to four hundred μg/g N (Fukuyama et al., 2020). Nevertheless, a large portion of the NH_4^+ component released from the involved potassium silicates will be dissolved into fluids. N that is stored in the fluid phase will be eventually recycled to the atmosphere through volcanic outgassing.
2. If N-bearing phases can be exhausted by Fe, Fe first reacts with the free water of fluids or the structural water of potassium silicates, and then bonds with N (Figure 9a). In such case, the hollandite-structured phase does not form, and the metallic Fe incorporates the majority of N released from its initial hosts. Fe nitrides and the N-bearing metallic melt are typically denser than the surrounding mantle. They might drain readily or stay trapped in the solid matrix depending on the viscosities of these materials. It is possible that Fe nitrides are carried to shallow regions through mantle convection or by mantle plume, as evidenced from nitride-bearing inclusions in superdeep diamonds (Kaminsky & Wirth, 2017). It is more likely that N-bearing metallic phases reside in the reduced mantle and are not recycled to the surface.

From two cases presented above, we can find that the recycling efficiency of subducted N is strongly related to the availability of the metallic Fe in the mantle. The more N bonded with Fe during slab-mantle interactions, the less

N will release back to the atmosphere through volcanic outgassing. The stabilization of Fe oxides over nitrides, however, limits Fe to alloy with N. Under anhydrous conditions, the metallic Fe of the reduced mantle is capable of concentrating N through slab-mantle interactions efficiently. While hydration of Fe-rich domains contributes to recycling N to the surface. In both cases, reactions of hydrous phases with Fe would increase the FeO contents of subducted slabs. This might contribute to a negative buoyancy that facilitates sedimentary materials to descend to increased depth or to be stagnant at the top of the mantle transition zone (Figure 9a).

5.2. Implications for Subducted Marine Sedimentary N

The mineralogical and isotopic characteristics of superdeep diamonds provide evidence for the recycling of oceanic crusts to lower-mantle depths (Nestola et al., 2018). A large amount of N in subducted marine sediments escapes to the mantle wedge along a hot slab geotherm, and those can be carried to deeper regions along a cold slab geotherm (Massonne & Fockenberg, 2022; Mysen, 2019; Zheng & Chen, 2016). However, the reactions of N-bearing phases with Fe of the reduced mantle may be impaired owing to water-rich features of subducted oceanic materials. The subducted marine sediments should transport surficial N to the metallic Fe less efficiently than subducted continental sediments.

During subduction, carbonates are also considered to be carried to the Earth′s interior and could be reduced by Fe to form diamonds below 250 km, which is one of the most important mechanisms for the genesis of superdeep diamonds (Nestola et al., 2018; Smith et al., 2016). It is widely accepted that N contents in most of superdeep diamonds are as low as several μg/g on average, which is explained by N partitioning into the metallic phase (Smith et al., 2016). For instance, the average N concentration is approximately 17 μg/g in lower-mantle diamonds (Smith & Kopylova, 2014). Considering the partition coefficient of N between diamond and Fe ranges from 0.01 to 0.0005, the N concentration in the coexisting metallic Fe should be 0.17∼3.4 wt% (Kaminsky & Wirth, 2017; Miyazaki et al., 2004). In addition, it is proposed that the lower mantle contains 1∼10 μg/g N (Johnson & Goldblatt, 2015). N strongly partitions into the metallic phase in comparison with coexisting mantle silicates with a partition coefficient of ∼100 (Yoshioka et al., 2018). The N concentration in the metallic Fe of the lower mantle should be 0.01∼0.1 wt% on average, much smaller than that of the metallic Fe coexisting with superdeep diamonds. This difference indicates a locally N-rich metallic domain near the subduction in comparison with those distributed in the entire lower mantle, which is likely attributed to the transportation of subducted N into this region. This also provides natural evidence for our conclusion that the metallic Fe of the reduced mantle is capable of concentrating N during slab-mantle interactions.

Kaminsky and Wirth (2017) have reported several Fe nitrides, carbonitrides and nitrocarbides as inclusions in lower-mantle diamonds. Whereas they are not observed in other superdeep diamonds, such as CLIPPIR diamonds (Smith et al., 2016). The heterogeneous distribution of nitrides in these diamonds cannot be explained solely by variations of formation depth. We notice that the N concentration is extremely low in CLIPPIR diamonds, in which the S-rich Fe-Ni-S-C melt is trapped. In contrast, there are not Fe sulfides or S-rich metallic melts trapped in most of superdeep diamonds observed by Kaminsky and Wirth (2017). In one lower-mantle diamond, where Fe sulfide exists, Fe nitride phases are not detected (Kaminsky et al., 2015).

The metallic Fe of the reduced mantle incorporates not only C and N but also S during slab-mantle interactions or during the crystallization of the magma ocean in the early Earth (Armstrong et al., 2019; Smith et al., 2016). The S concentration varies from less than 1 wt% to more than 10 wt% in the metallic Fe (Kaminsky & Wirth, 2017; Smith et al., 2016). If the metallic Fe contains less S, it could be predominantly in the solid state or become partially molten in the slab geotherm. During slab-mantle interactions, C and N in slabs react with the metallic Fe to form reduced species, such as Fe nitride, carbide, or diamond. Based on the relative stability of Fe-LEs, the incorporation of a small amount of S into the metallic Fe has a negligible effect on the bonding of N with Fe but contributes to expelling C to the C-rich region below solidus. In the meanwhile, Fe carbide can further react with N-bearing materials to form Fe carbonitride and diamond (Litasov et al., 2016). C and N are both compatible in the S-depleted metallic melt. When C becomes supersaturated to precipitate as diamond, N is nearly incompatible in the metallic melt and ready to form Fe nitride. In such case, C-bearing Fe nitride phases could be trapped as inclusions when diamonds are formed (Figure 9b). On the other hand, the metallic Fe could become fully molten if S is continuously supplied to it. The solubility of C in the Fe melt decreases significantly from ∼4 wt% to ∼0.3 wt% as S contents increase from 0 wt% to 25 wt% at pressures of 7∼10 GPa (Grewal et al., 2019; Zhang et al., 2019). The incorporation of S also reduces the solubility of N in the Fe melt, but this effect is less

pronounced. For instance, the solubility of N in the metallic melt containing 25 wt% S is ~1.5 wt%, five times higher than that of C (Grewal et al., 2019). With increasing S contents, C becomes supersaturated at relatively low concentrations, whereas N resides primarily in the Fe melt. As a consequence, Fe nitride phases are absent in superdeep diamonds but Fe sulfides could be detected in them (Figure 9b).

These processes imply that the heterogeneous distribution of N-bearing phases in superdeep diamonds may also reflect the chemical heterogeneity of formation environments of superdeep diamonds. In addition to physical conditions (i.e., *P* and *T*), the chemical environment imposes an equivalently important effect on the distribution of Fe nitride phases in superdeep diamonds. Moreover, our study highlights that the relative stability of Fe-LEs at high *P-T* conditions plays a key role in the storage and evolution of volatiles in the metallic Fe of the reduced mantle, which helps to decipher the phase assemblages observed in superdeep diamonds, and to understand the coupled or decoupled cycles of deep volatiles. Further investigations on the relative stability of Fe-LEs over much broader *P-T* ranges are required in order to constrain the storage and evolution of volatiles in the deep lower mantle.

Data Availability Statement

All the data necessary to produce the results are available on Zenodo (http://doi.org/10.5281/zenodo.6813906).

Acknowledgments
The authors acknowledge the financial support from the National Natural Science Foundation of China (NSFC) grants (41473056 and 41827802) to X. Wu, NSFC-42072047 to S. Qin, and U.S.A. National Science Foundation (NSF) grants (EAR-1555388 and EAR-2127807) to B. Chen. S. Huang acknowledges support from Peking University Boya Postdoctoral Fellowship and China Postdoctoral Science Foundation (No. 2022M710194). The authors thank Jingjing Niu for his help in nitrogen gas loading. Part of experiments in this research were performed at GeoSoilEnviroCARS (Sector 13), Advanced Photon Source (APS), Argonne National Laboratory (ANL). GeoSoilEnviroCARS is supported by the National Science Foundation-Earth Sciences (EAR-1634415) and Department of Energy-GeoSciences (DE-FG02-94ER14466). This research used resources of the APS, a U.S. Department of Energy (DOE) Office of Science User Facility operated for the DOE Office of Science by ANL under Contract No. DE-AC02-06CH11357. Part of experiments in this research were performed at beamline 15U of Shanghai Synchrotron Radiation Facility (SSRF) and at beamline 4W2 of Beijing Synchrotron Radiation Facility (BSRF). The authors thank the Supercomputing Laboratory of IGGCAS (Institute of Geology and Geophysics, Chinese Academy of Sciences) for the computational resources and support.

References

Antonov, V. E., Cornell, K., Fedotov, V. K., Kolesnikov, A. I., Ponyatovsky, E. G., Shiryaev, V. I., & Wipf, H. (1998). Neutron diffraction investigation of the dhcp and hcp iron hydrides and deuterides. *Journal of Alloys and Compounds*, *264*(1–2), 214–222. https://doi.org/10.1016/S0925-8388(97)00298-3

Armstrong, K., Frost, D. J., McCammon, C. A., Rubie, D. C., & Ballaran, T. B. (2019). Deep magma ocean formation set the oxidation state of Earth′s mantle. *Science*, *365*(6456), 903–906. https://doi.org/10.1126/science.aax8376

Barry, P., & Hilton, D. R. (2016). Release of subducted sedimentary nitrogen throughout Earth's mantle. *Geochemical Perspectives Letters*, *2*(2), 148–159. https://doi.org/10.7185/geochemlet.1615

Bekaert, D. V., Turner, S. J., Broadley, M. W., Barnes, J. D., Halldórsson, S. A., Labidi, J., et al. (2021). Subduction-driven volatile recycling: A global mass balance. *Annual Review of Earth and Planetary Sciences*, *49*, 37–70. https://doi.org/10.1146/annurev-earth-071620-055024

Busigny, V., Cartigny, P., & Philippot, P. (2011). Nitrogen isotopes in ophiolitic metagabbros: A re-evaluation of modern nitrogen fluxes in subduction zones and implication for the early Earth atmosphere. *Geochimica et Cosmochimica Acta*, *75*(23), 7502–7521. https://doi.org/10.1016/j.gca.2011.09.049

Busigny, V., Cartigny, P., Philippot, P., Ader, M., & Javoy, M. (2003). Massive recycling of nitrogen and other fluid-mobile elements (K, Rb, Cs, H) in a cold slab environment: Evidence from HP to UHP oceanic metasediments of the Schistes Lustrés nappe (western Alps, Europe). *Earth and Planetary Science Letters*, *215*(1–2), 27–42. https://doi.org/10.1016/S0012-821X(03)00453-9

Busigny, V., Cartigny, P., Philippot, P., & Javoy, M. (2003). Ammonium quantification in muscovite by infrared spectroscopy. *Chemical Geology*, *198*(1–2), 21–31. https://doi.org/10.1016/S0009-2541(02)00420-5

Chen, S., Guo, X., Yoshino, T., Jin, Z., & Li, P. (2018). Dehydration of phengite inferred by electrical conductivity measurements: Implication for the high conductivity anomalies relevant to the subduction zones. *Geology*, *46*(1), 11–14. https://doi.org/10.1130/G39716.1

Dorogokupets, P. I., & Dewaele, A. (2007). Equations of state of MgO, Au, Pt, NaCl-B1, and NaCl-B2: Internally consistent high-temperature pressure scales. *High Pressure Research*, *27*(4), 431–446. https://doi.org/10.1080/08957950701659700

Dudarev, S. L., Botton, G. A., Savrasov, S. Y., Humphreys, C. J., & Sutton, A. P. (1998). Electron-energy-loss spectra and the structural stability of nickel oxide: An LSDA+*U* study. *Physical Review B*, *57*(3), 1505–1509. https://doi.org/10.1103/PhysRevB.57.1505

Fei, Y., Bertka, C. M., & Finger, L. W. (1997). High-pressure iron-sulfur compound, Fe_3S_2, and melting relations in the Fe-FeS system. *Science*, *275*(5306), 1621–1623. https://doi.org/10.1126/science.275.5306.1621

Fei, Y., Li, J., Bertka, C. M., & Prewitt, C. T. (2000). Structure type and bulk modulus of Fe_3S, a new iron-sulfur compound. *American Mineralogist*, *85*(11–12), 1830–1833. https://doi.org/10.2138/am-2000-11-1229

Fischer, R. A., Campbell, A. J., Shofner, G. A., Lord, O. T., Dera, P., & Prakapenka, V. B. (2011). Equation of state and phase diagram of FeO. *Earth and Planetary Science Letters*, *304*(3–4), 496–502. https://doi.org/10.1016/j.epsl.2011.02.025

Fukuyama, K., Kagi, H., Inoue, T., Kakizawa, S., Shinmei, T., Hishita, S., et al. (2020). High nitrogen solubility in stishovite (SiO_2) under lower mantle conditions. *Scientific Reports*, *10*, 10897. https://doi.org/10.1038/s41598-020-67621-2

Grewal, D. S., Dasgupta, R., Sun, C., Tsuno, K., & Costin, G. (2019). Delivery of carbon, nitrogen, and sulfur to the silicate Earth by a giant impact. *Science Advances*, *5*(1), eaau3669. https://doi.org/10.1126/sciadv.aau3669

Hao, M., Zhang, J. S., Pierotti, C. E., Zhou, W. Y., Zhang, D., & Dera, P. (2020). The seismically fastest chemical heterogeneity in the Earth′s deep upper mantle-implications from the single-crystal thermoelastic properties of jadeite. *Earth and Planetary Science Letters*, *543*, 116345. https://doi.org/10.1016/j.epsl.2020.116345

Huang, S., Wu, X., & Qin, S. (2018). Ultrahigh-pressure phase transitions in FeS_2 and FeO_2: Implications for super-Earths′ deep interior. *Journal of Geophysical Research: Solid Earth*, *123*, 277–284. https://doi.org/10.1002/2017JB014766

Huang, S., Wu, X., Zhu, F., Lai, X., Li, J., Neill, O. K., et al. (2021). High-pressure phase stability and thermoelastic properties of iron carbonitrides and nitrogen in the deep Earth. *Journal of Geophysical Research: Solid Earth*, *126*, e2021JB021934. https://doi.org/10.1029/2021JB021934

Huang, W., Yang, Y., Qi, Z., Liu, W., Wang, Z., Liu, Y., & Xia, Q. (2021). Ammonium impacts on vibrations of hydroxyl and lattice of phengite at high temperature and high pressure. *Journal of Earth Science*, *32*, 1278–1286. https://doi.org/10.1007/s12583-020-1113-4

Jackson, C. R., Cottrell, E., & Andrews, B. (2021). Warm and oxidizing slabs limit ingassing efficiency of nitrogen to the mantle. *Earth and Planetary Science Letters*, *553*, 116615. https://doi.org/10.1016/j.epsl.2020.116615

Johnson, B., & Goldblatt, C. (2015). The nitrogen budget of Earth. *Earth-Science Reviews*, *148*, 150–173. https://doi.org/10.1016/j.earscirev.2015.05.006

Kaminsky, F. V., & Wirth, R. (2017). Nitrides and carbonitrides from the lowermost mantle and their importance in the search for Earth′s "lost" nitrogen. *American Mineralogist*, *102*(8), 1667–1676. https://doi.org/10.2138/am-2017-6101

Kaminsky, F. V., Wirth, R., & Schreiber, A. (2015). A microinclusion of lower-mantle rock and other mineral and nitrogen lower-mantle inclusions in a diamond. *The Canadian Mineralogist*, *53*(1), 83–104. https://doi.org/10.3749/canmin.1400070

Kresse, G., & Joubert, D. (1999). From ultrasoft pseudopotentials to the projector augmented-wave method. *Physical Review B*, *59*(3), 1758–1775. https://doi.org/10.1103/PhysRevB.59.1758

Labidi, J., Barry, P. H., Bekaert, D. V., Broadley, M. W., Marty, B., Giunta, T., et al. (2020). Hydrothermal $^{15}N^{15}N$ abundances constrain the origins of mantle nitrogen. *Nature*, *580*(7803), 367–371. https://doi.org/10.1038/s41586-020-2173-4

Lai, X., Zhu, F., Gao, J., Greenberg, E., Prakapenka, V. B., Meng, Y., & Chen, B. (2022). Melting of the Fe-C-H system and Earth′s deep carbon-hydrogen cycle. *Geophysical Research Letters*, *49*(13), e2022GL098919. https://doi.org/10.1029/2022GL098919

Li, K., Li, G. Y., Du, Y. F., Han, W., Zhang, J., Chen, L. H., et al. (2021). Intraslab remobilization of nitrogen during early subduction facilitates deep nitrogen recycling: Insights from the blueschists in the Heilongjiang Complex in NE China. *Chemical Geology*, *583*, 120474. https://doi.org/10.1016/j.chemgeo.2021.120474

Li, Y., Wiedenbeck, M., Shcheka, S., & Keppler, H. (2013). Nitrogen solubility in upper mantle minerals. *Earth and Planetary Science Letters*, *377*, 311–323. https://doi.org/10.1016/j.epsl.2013.07.013

Litasov, K. D., Shatskiy, A., Ponomarev, D. S., & Gavryushkin, P. N. (2017). Equations of state of iron nitrides ε-Fe_3N_x and γ-Fe_4N_y to 30 GPa and 1200 K and implication for nitrogen in the Earth′s core. *Journal of Geophysical Research: Solid Earth*, *122*(5), 3574–3584. https://doi.org/10.1002/2017JB014059

Litasov, K. D., Shatskiy, A. F., & Ohtani, E. (2016). Interaction of Fe and Fe_3C with hydrogen and nitrogen at 6–20 GPa: A study by in situ X-ray diffraction. *Geochemistry International*, *54*(10), 914–921. https://doi.org/10.1134/S0016702916100074

Liu, J., Dubrovinsky, L., Boffa Ballaran, T., & Crichton, W. (2007). Equation of state and thermal expansivity of LiF and NaF. *High Pressure Research*, *27*(4), 483–489. https://doi.org/10.1080/08957950701684690

Liu, L., Zhang, J., Green II H. W., Jin, Z., & Bozhilov, K. N. (2007). Evidence of former stishovite in metamorphosed sediments, implying subduction to > 350 km. *Earth and Planetary Science Letters*, *263*(3–4), 180–191. https://doi.org/10.1016/j.epsl.2007.08.010

Liu, W., Yang, Y., Busigny, V., & Xia, Q. K. (2019). Intimate link between ammonium loss of phengite and the deep Earth′s water cycle. *Earth and Planetary Science Letters*, *513*, 95–102. https://doi.org/10.1016/j.epsl.2019.02.022

Lv, C., & Liu, J. (2022). Ultralow melting of iron nitrides and the Fe-N-C system at high pressure. *Journal of Geophysical Research: Solid Earth*, *127*(2), e2021JB023718. https://doi.org/10.1029/2021JB023718

Massonne, H. J., & Fockenberg, T. (2022). Melting of phengite-bearing eclogite at pressures of 4 and 9 GPa relevant to deep regions of a subduction zone. *Earth and Planetary Science Letters*, *584*, 117475. https://doi.org/10.1016/j.epsl.2022.117475

Mikhail, S., & Sverjensky, D. A. (2014). Nitrogen speciation in upper mantle fluids and the origin of Earth′s nitrogen-rich atmosphere. *Nature Geoscience*, *7*(11), 816–819. https://doi.org/10.1038/ngeo2271

Minobe, S., Nakajima, Y., Hirose, K., & Ohishi, Y. (2015). Stability and compressibility of a new iron-nitride β-Fe_7N_3 to core pressures. *Geophysical Research Letters*, *42*(13), 5206–5211. https://doi.org/10.1002/2015GL064496

Miyazaki, A., Hiyagon, H., Sugiura, N., Hirose, K., & Takahashi, E. (2004). Solubilities of nitrogen and noble gases in silicate melts under various oxygen fugacities: Implications for the origin and degassing history of nitrogen and noble gases in the Earth. *Geochimica et Cosmochimica Acta*, *68*(2), 387–401. https://doi.org/10.1016/S0016-7037(03)00484-8

Mookherjee, M., Nakajima, Y., Steinle-Neumann, G., Glazyrin, K., Wu, X., Dubrovinsky, L., et al. (2011). High-pressure behavior of iron carbide (Fe_7C_3) at inner core conditions. *Journal of Geophysical Research*, *116*(B4), B04201. https://doi.org/10.1029/2010JB007819

Mysen, B. (2019). Nitrogen in the Earth: Abundance and transport. *Progress in Earth and Planetary Science*, *6*(1), 1–15. https://doi.org/10.1186/s40645-019-0286-x

Narygina, O., Dubrovinsky, L. S., McCammon, C. A., Kurnosov, A., Kantor, I. Y., Prakapenka, V. B., & Dubrovinskaia, N. A. (2011). X-ray diffraction and Mössbauer spectroscopy study of fcc iron hydride FeH at high pressures and implications for the composition of the Earth′s core. *Earth and Planetary Science Letters*, *307*(3–4), 409–414. https://doi.org/10.1016/j.epsl.2011.05.015

Navon, O., Wirth, R., Schmidt, C., Jablon, B. M., Schreiber, A., & Emmanuel, S. (2017). Solid molecular nitrogen (δ-N_2) inclusions in Juina diamonds: Exsolution at the base of the transition zone. *Earth and Planetary Science Letters*, *464*, 237–247. https://doi.org/10.1016/j.epsl.2017.01.035

Nestola, F., Korolev, N., Kopylova, M., Rotiroti, N., Pearson, D. G., Pamato, M. G., et al. (2018). $CaSiO_3$ perovskite in diamond indicates the recycling of oceanic crust into the lower mantle. *Nature*, *555*(7695), 237–241. https://doi.org/10.1038/nature25972

Perdew, J. P., Burke, K., & Ernzerhof, M. (1996). Generalized gradient approximation made simple. *Physical Review Letters*, *77*(18), 3865–3868. https://doi.org/10.1103/PhysRevLett.77.3865

Piet, H., Leinenweber, K., Greenberg, E., Prakapenka, V. B., & Shim, S. H. (2021). Effects of hydrogen on the phase relations in Fe-FeS at pressures of Mars-sized bodies. *Journal of Geophysical Research: Planets*, *126*(11), e2021JE006942. https://doi.org/10.1029/2021JE006942

Prakapenka, V. B., Kubo, A., Kuznetsov, A., Laskin, A., Shkurikhin, O., Dera, P., et al. (2008). Advanced flat top laser heating system for high pressure research at GSECARS: Application to the melting behavior of germanium. *High Pressure Research*, *28*(3), 225–235. https://doi.org/10.1080/08957950802050718

Rohrbach, A., Ballhaus, C., Golla-Schindler, U., Ulmer, P., Kamenetsky, V. S., & Kuzmin, D. V. (2007). Metal saturation in the upper mantle. *Nature*, *449*(7161), 456–458. https://doi.org/10.1038/nature06183

Schmidt, M. W. (1996). Experimental constraints on recycling of potassium from subducted oceanic crust. *Science*, *272*(5270), 1927–1930. https://doi.org/10.1126/science.272.5270.1927

Schmidt, M. W., & Poli, S. (1998). Experimentally based water budgets for dehydrating slabs and consequences for arc magma generation. *Earth and Planetary Science Letters*, *163*(1–4), 361–379. https://doi.org/10.1016/S0012-821X(98)00142-3

Schmidt, M. W., Vielzeuf, D., & Auzanneau, E. (2004). Melting and dissolution of subducting crust at high pressures: The key role of white mica. *Earth and Planetary Science Letters*, *228*(1–2), 65–84. https://doi.org/10.1016/j.epsl.2004.09.020

Schwarz, U., Wosylus, A., Wessel, M., Dronskowski, R., Hanfland, M., Rau, D., & Niewa, R. (2009). High-pressure-high-temperature behavior of ζ-Fe_2N and phase transition to ε-$Fe_3N_{1.5}$. *European Journal of Inorganic Chemistry*, *2009*(12), 1634–1639. https://doi.org/10.1002/ejic.200801222

Shibazaki, Y., Ohtani, E., Terasaki, H., Tateyama, R., Sakamaki, T., Tsuchiya, T., & Funakoshi, K. I. (2011). Effect of hydrogen on the melting temperature of FeS at high pressure: Implications for the core of Ganymede. *Earth and Planetary Science Letters*, *301*(1–2), 153–158. https://doi.org/10.1016/j.epsl.2010.10.033

Smith, E. M., & Kopylova, M. G. (2014). Implications of metallic iron for diamonds and nitrogen in the sublithospheric mantle. *Canadian Journal of Earth Sciences*, *51*(5), 510–516. https://doi.org/10.1139/cjes-2013-0218

Smith, E. M., Shirey, S. B., Nestola, F., Bullock, E. S., Wang, J., Richardson, S. H., & Wang, W. (2016). Large gem diamonds from metallic liquid in Earth's deep mantle. *Science*, *354*(6318), 1403–1405. https://doi.org/10.1126/science.aal1303

Sokol, A. G., Sokol, E. V., Kupriyanov, I. N., & Sobolev, N. V. (2018). Synthesis of NH_4-substituted muscovite at 6.3 GPa and 1000°C: Implications for nitrogen transport to the Earth's mantle. *Doklady Earth Sciences*, *479*(1), 404–407. https://doi.org/10.1134/S1028334X18030315

Speelmanns, I. M., Schmidt, M. W., & Liebske, C. (2018). Nitrogen solubility in core materials. *Geophysical Research Letters*, *45*(15), 7434–7443. https://doi.org/10.1029/2018GL079130

Tagawa, S., Ohta, K., Hirose, K., Kato, C., & Ohishi, Y. (2016). Compression of Fe-Si-H alloys to core pressures. *Geophysical Research Letters*, *43*(8), 3686–3692. https://doi.org/10.1002/2016GL068848

Watenphul, A., Wunder, B., & Heinrich, W. (2009). High-pressure ammonium-bearing silicates: Implications for nitrogen and hydrogen storage in the Earth's mantle. *American Mineralogist*, *94*(2–3), 283–292. https://doi.org/10.2138/am.2009.2995

Wu, Y., Fei, Y., Jin, Z., & Liu, X. (2009). The fate of subducted upper continental crust: An experimental study. *Earth and Planetary Science Letters*, *282*(1–4), 275–284. https://doi.org/10.1016/j.epsl.2009.03.028

Xu, J., Zhang, D., Fan, D., Dera, P. K., Shi, F., & Zhou, W. (2019). Thermoelastic properties of eclogitic garnets and omphacites: Implications for deep subduction of oceanic crust and density anomalies in the upper mantle. *Geophysical Research Letters*, *46*(1), 179–188. https://doi.org/10.1029/2018GL081170

Yoshioka, T., Wiedenbeck, M., Shcheka, S., & Keppler, H. (2018). Nitrogen solubility in the deep mantle and the origin of Earth′s primordial nitrogen budget. *Earth and Planetary Science Letters*, *488*, 134–143. https://doi.org/10.1016/j.epsl.2018.02.021

Zhang, Z., Qin, T., Pommier, A., & Hirschmann, M. M. (2019). Carbon storage in Fe-Ni-S liquids in the deep upper mantle and its relation to diamond and Fe-Ni alloy precipitation. *Earth and Planetary Science Letters*, *520*, 164–174. https://doi.org/10.1016/j.epsl.2019.05.039

Zheng, Y. F., & Chen, Y. X. (2016). Continental versus oceanic subduction zones. *National Science Review*, *3*(4), 495–519. https://doi.org/10.1093/nsr/nww049

Zhu, F., Li, J., Liu, J., Dong, J., & Liu, Z. (2019). Metallic iron limits silicate hydration in Earth's transition zone. *Proceedings of the National Academy of Sciences*, *116*(45), 22526–22530. https://doi.org/10.1073/pnas.1908716116